Soft Matter

PAPER

View Article Online
View Journal

Cite this: DOI: 10.1039/d6sm00092d

3D morphology and phase-selective transport in amphiphilic silicone hydrogels: experiments and multiscale simulations

Eri Ito,*[ab] Yoshiaki Kawagoe *[a] and Tomonaga Okabe[cde]

Amphiphilic bicontinuous nanophase-separated networks can, in principle, provide independent pathways for transporting hydrophobic and hydrophilic species, yet PIPS membranes still lack a tightly validated link between 3D domain connectivity, domain identity, and phase-selective transport. Here, we study amphiphilic silicone hydrogels formed by PIPS from hydrophobic silicone segments and hydrophilic monomers using complementary experiments and multiscale modeling. TEM combined with Fourier analysis resolves nanoscale phase separation, and 3D TEM reconstruction supports a bicontinuous morphology in a representative ternary formulation, providing insight into domain connectivity and composition. To connect structure and function, we measure permeability trends using oxygen as a probe for silicone-rich pathways and sodium ions as a probe for the hydrophilic network, revealing composition-dependent, phase-specific transport. To rationalize morphology formation, key interaction descriptors are extracted from all-atom molecular dynamics and transferred to reactive dissipative particle dynamics simulations of PIPS, yielding domain features consistent with experiments. Finally, domain-restricted random-walk analyses capture the phase-dependent diffusion trends and show that transport selectivity cannot be explained by the domain volume fraction alone; instead, pathway geometry (*e.g.*, tortuosity), which depends on monomer identity, makes a key contribution. Together, these results establish an experiment–simulation workflow linking molecular interactions to 3D morphology and selective transport, enabling the simulation-guided design of amphiphilic membranes.

Received 3rd February 2026,
Accepted 26th May 2026

DOI: 10.1039/d6sm00092d

rsc.li/soft-matter-journal

1 Introduction

Bicontinuous structures, characterized by two or more interpenetrating continuous phases, represent a unique class of morphologies primarily formed in polymeric systems.[1] These structures offer significant advantages for tuning and enhancing a wide range of material properties, including mechanical strength, thermal stability, chemical resistance, electrical conductivity, and optical transparency. Thus, bicontinuous architectures have attracted considerable interest as a design strategy for multifunctional materials capable of resolving the trade-offs between conflicting requirements. Notable examples include lightweight yet strong aerospace materials, electrochemical devices such as fuel cells that require both electronic and ionic conductivity,[2] and porous membranes for water purification or gas separation where both permeability and selectivity must be optimized.

Various methods have been developed to fabricate bicontinuous structures in polymeric materials. Traditional approaches include the use of polymer blends, block copolymers, and organic–inorganic hybrids, where each component is predesigned and structurally controlled. In contrast, polymerization-induced phase separation (PIPS),[3] a process in which the progression of polymerization or crosslinking reactions triggers spontaneous spinodal decomposition,[4] offers a more integrated and potentially scalable approach. In PIPS, the material undergoes concurrent chemical reactions and structural formation, providing practical advantages for industrial applications.

Despite its promise, PIPS-derived bicontinuous morphologies are inherently difficult to analyze and control owing to the dynamic and reaction-coupled nature of phase separation. Unlike

[a] Research Center for Green X-Tech, Tohoku University, 6-6-11, Aoba, Aramaki, Aoba-ku, Sendai, 980-8579, Japan. E-mail: eri.ito.e5@tohoku.ac.jp, kawagoe@tohoku.ac.jp
[b] Co-Creation Strategy Department, Menicon Co. Ltd, 3-21-19 Aoi, Naka-ku, Nagoya, 460-0006, Japan
[c] Department of Aerospace Engineering, Tohoku University, 6-6-01, Aoba, Aramaki, Aoba-ku, Sendai, 980-8579, Japan
[d] Department of Materials Science and Engineering, University of Washington, BOX 352120, Seattle, WA, 98195-1750, USA
[e] Research Center for Structural Materials, Polymer Matrix Hybrid Composite Materials Group, National Institute for Materials Science, 1-2-1 Sengen, Tsukuba, Ibaraki, 305-0047, Japan

block copolymers or blends with predefined architectures, PIPS involves simultaneous reaction kinetics and phase behavior, complicating structural characterization. However, recent advances in high-resolution structural analysis techniques, including small-angle X-ray and neutron scattering (SAXS/SANS) and transmission electron microscopy (TEM),[5] can elucidate the formation mechanisms and hierarchical structures of these complex materials. Moreover, these morphological observations require an understanding of the topology.

Computational approaches for simulating phase-separation dynamics have advanced considerably in recent years. Field-based methods such as dynamic self-consistent field theory[6,7] and particle-based methods, including coarse-grained molecular dynamics[8,9] and dissipative particle dynamics (DPD)[10,11] have been widely adopted. Among these, DPD is particularly powerful for modeling large-scale phase behavior while incorporating atomic-level information through bottom-up parameterization.[12–14] Furthermore, DPD combined with reaction models has enabled simulations of polymerization- or reaction-induced phase separation, successfully reproducing morphology development based on material composition and reaction conditions.[15,16]

A representative application of bicontinuous polymer structures is soft contact lenses. Designed for vision correction, these lenses adhere to the corneal surface *via* tear fluid surface tension and require high oxygen and ion permeabilities to maintain ocular health. Since the introduction of water-swollen hydrogel-based lenses in the 1960s, recent developments have focused on materials with enhanced oxygen permeability. The current standard is a silicone hydrogel (SiHy),[17,18] an amphiphilic network composed of hydrophilic monomers and silicone-containing components with siloxane linkages. These materials form mesoscopically phase-separated structures[19] that combine the oxygen permeability of the silicone domains with the hydrophilicity necessary for comfort and biocompatibility.

Structural analyses using SAXS, SANS, and TEM have confirmed the presence of bicontinuous morphologies in SiHy materials.[20] Moreover, the SiHy phase-separated network enables efficient molecular transport, further validating its bicontinuous nature.

In this study, we investigated the phase separation behavior and resulting morphologies of SiHy materials composed of the representative monomers polydimethylsiloxane-α,ω-diacrylate (PDMS), tris-(trimethylsiloxy)-3-(methacryloxy)propylsilane (TMSM), and *N*,*N*′-dimethylacrylamide (DMAA). Both binary (PDMS/DMAA) and ternary systems[21] were investigated, and the PIPS morphologies were characterized by TEM, including three-dimensional TEM reconstruction. The transport properties of the resulting phase-separated structures were evaluated experimentally. In addition, both the binary and ternary systems were modeled using reactive DPD simulations to enable numerical evaluation of the corresponding transport properties. Our primary goal was to elucidate the relationship between material composition, phase-separated structure, and transport properties. By comparing the experimentally observed morphologies with simulated phase separation and structure–property analyses, we aim to provide a deeper understanding of the mesoscale architecture and its functional implications in SiHy materials.

2 Experimental analysis method

2.1 Materials

Reactive telechelic PDMS with the structure shown in Fig. 1 was synthesized[21] and has a molecular weight of 6500 g mol^{-1} and a polydispersity of 1.5 as determined by size exclusion chromatography (the columns were calibrated by polystyrene standards). TMSM was purchased from Shin-Etsu Chemical Co., Ltd (Japan) and DMAA was purchased from KJ Chemicals Corporation (Japan). TMSM and DMAA were purified *via* distillation under vacuum.

Amphiphilic polymers were synthesized using DMAA, PDMS, and TMSM, in the ratios listed in Table 1. Each component was mixed with 0.5 wt% ethylene dimethacrylate and 0.1 wt% 2,2′-azobis(2,4-dimethylvaleronitrile), followed by thorough mixing and deoxygenation. The mixtures were placed in test tubes, which were then immersed in water baths set to 35 °C for 40 h, and subsequently at 50 °C for 8 h to perform free-radical polymerization.

2.2 Transmission electron microscopy (TEM) observation

The phase-separated structures of amphiphilic polymer films were examined *via* TEM. For samples 1–3, ultrathin cryosections approximately 100 nm thick were prepared using a cryo-ultramicrotome (Leica) and subsequently stained by exposure to ruthenium tetroxide vapor prior to TEM observation. Sample 4 was processed into a rod-shaped specimen with dimensions of approximately 2 × 2 × 6 μm using a focused ion beam (FIB, FEI) operated at 30 kV Ga ion irradiation. Each specimen was lifted using a tungsten microprobe and mounted on a TEM grid. Because the phase-separated domain size of sample 4 was smaller than that of the other samples, the staining protocol was optimized to enhance the electron contrast. Specifically, the specimen was immersed in a 10% aqueous solution of phosphotungstic acid (PTA) for 6 h to ensure sufficient penetration of PTA into the rod interior and achieve adequate contrast. DMAA-containing regions exhibited darker contrast in TEM images following staining with 10% PTA.

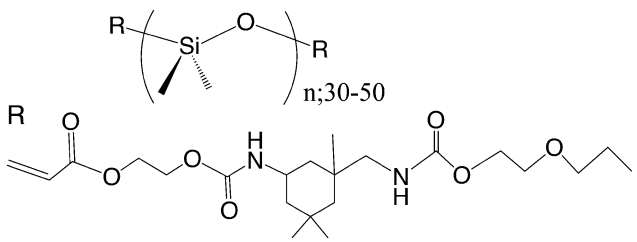

Fig. 1 Chemical structure of the reactive PDMS macromonomer used in this study, bearing a polymerizable acrylate group and a PDMS segment (n = 30–50).[21]

Table 1 Weight fraction components in the amphiphilic copolymer

	PDMS [%]	TMSM [%]	DMAA [%]
Sample 1: p(PDMS/DMAA)1	80	—	20
Sample 2: p(PDMS/DMAA)2	60	—	40
Sample 3: p(PDMS/DMAA)3	40	—	60
Sample 4: p(PDMS/TMSM/DMAA)	34	33	33

Three-dimensional (3D) TEM imaging[22] of sample 4 was performed using a JEM-1400 transmission electron microscope (JEOL Ltd) operated at an accelerating voltage of 200 kV. Projection images were automatically acquired with a Gatan Orius slow-scan CCD camera controlled using Inspect3D software while tilting the specimen in 1° increments up to 90°. The initial magnification for TEM imaging was set to 100 000×.

2.3 Physical transport

2.3.1 Ion permeability measurements. The permeability of NaCl through amphiphilic copolymer membranes was measured using a temperature-controlled Pyrex glass permeation cell maintained at 35 ± 0.1 °C. The membrane was placed between the two compartments of the cell. A 0.1 M aqueous NaCl solution was introduced into one compartment (donor side), and salt-free distilled water was placed in the other compartment (permeate side). The time-dependent change in NaCl concentration on the permeate side was monitored using a conductivity meter, and the NaCl permeability coefficient P_S was determined from a calibration curve correlating NaCl concentration with conductivity.[23]

The time-dependent change in NaCl concentration was measured in the acceptor-side cell, and the NaCl concentration was plotted as a function of time. The NaCl flux through the membrane, J_S (mol cm^{-2} s^{-1}), was determined from the slope of the linear region of the resulting plot. In this study, the effective permeation area is defined as the area corresponding to the water-swollen hydrophilic domains of the membrane, assuming that this area is proportional to the volume of the swollen hydrophilic domains.

The NaCl permeability coefficient P_S (cm^2 s^{-1}) was calculated using the following equation:

$$P_S = \frac{J_S \cdot L}{\Delta C} \tag{1}$$

where L is the membrane thickness and ΔC is the NaCl concentration difference across the membrane.

2.3.2 Oxygen permeability measurements. This measurement was performed in accordance with ISO 18369-4: ophthalmic optics–contact lenses–Part 4: physicochemical properties of contact lens materials. Oxygen permeability was measured using a coulometric oxygen permeability analyzer (Dk1000, Chiron Technology, USA).

2.3.2.1 Measurement conditions. The measurement environment was as follows:

- Temperature: 35.0 ± 0.5 °C
- Carrier gas (N_2) flow rate: 15 mL min^{-1}
- O_2 flow rate: 15 mL min^{-1}
- Reference material: Menicon EX (reference D_k = 64 × 10^{-11} cm^2 s^{-1} mL O_2 (mL mmHg)$^{-1}$)

2.3.2.2 Measurement procedure. 1. The sample thickness was measured at ten different positions using a micrometer (OMV-25DM, Mitutoyo Corp.) and the average value was used.

2. The sample or reference lens was mounted in the sample cell.

3. A magnetic stirrer was placed on the sample cell and was operated at approximately 600 rpm.

4. The N_2 flow was set to approximately 50 mL min^{-1} to purge the cell. Humidified nitrogen (passed through distilled water, relative humidity = 100%) was used.

5. After 5 min, the N_2 flow was reduced to 15 mL min^{-1} and was maintained for an additional 1–2 min.

6. The chart recorder was activated. The lower cell valve was switched to the sensor side, and the stabilized zero voltage, V_0 (mV), was recorded to three decimal places.

7. The O_2 flow was adjusted to approximately 15 mL min^{-1} and the upper cell valve was switched to the oxygen purge side.

8. Once stabilized, the steady-state voltage, V_e (mV), was recorded to three decimal places and the atmospheric pressure was measured to 0.1 mmHg.

9. Steps 1–8 were repeated for both the reference material and the sample.

2.3.2.3 Calculation of oxygen permeability. The value of $(V{\cdot}t/P)$ was calculated using the following equation:

$$\frac{V \cdot t}{P} = \frac{(V_e - V_0)t}{P} \tag{2}$$

where V_e is the steady-state voltage (mV), V_0 is the zero voltage (mV), t is the sample thickness (cm), and P is the atmospheric pressure (mmHg). The oxygen permeability (D_k) was calculated using the following equation:

$$D_k = (V \cdot t/P)_{\text{sample}} \times \frac{D_{k,\text{ref}}}{(V \cdot t/P)_{\text{ref}}} \tag{3}$$

where $D_{k,\text{ref}}$ is the D_k-value of Menicon EX.

3 Numerical analysis method

The polymerization of SiHy was reproduced *via* a polymerization DPD simulation. The DPD parameters were determined bottom-up from all-atom molecular dynamics (MD) simulations, considering the effects of the molecular structure. This procedure is described in detail below.

3.1 DPD parametrization

DPD is a coarse-grained approach that enables simulations at larger spatiotemporal scales than all-atom MD simulations. The time evolution of DPD beads followed Newton's equations of motion, and the forces acting on them are expressed as follows:

$$\mathbf{f}_i = \sum_{i \neq j} \left(\mathbf{F}_{ij}^{C} + \mathbf{F}_{ij}^{D} + \mathbf{F}_{ij}^{R} \right) + \sum_{\text{bonds with } i} \mathbf{F}_i^{B} \tag{4}$$

Here, $\boldsymbol{F}_{ij}^{C}$ is the conservative force between beads i and j, which is represented by the following soft repulsion:

$$\mathbf{F}_{ij}^{C} = \frac{a_{ij}}{r_c} \omega(r_{ij}) \hat{\mathbf{r}}_{ij} \tag{5}$$

$$\omega(r_{ij}) = \begin{cases} 1 - \dfrac{r_{ij}}{r_c} & (r_{ij} < r_c), \\ 0 & (r_{ij} \geq r_c), \end{cases} \tag{6}$$

where a_{ij} is the pairwise repulsion parameter; r_c is the cutoff distance; and $\hat{\mathbf{r}}_{ij} = \mathbf{r}_{ij}/r_{ij}$ is the unit vector from bead j to bead i, where $\mathbf{r}_{ij} = \mathbf{r}_i - \mathbf{r}_j$ and $r_{ij} = |\mathbf{r}_{ij}|$. The dissipative force $\mathbf{F}_{ij}^{D}$ and random force $\mathbf{F}_{ij}^{R}$ represent the viscous drag and thermal noise, respectively; the conventional functional forms and parameters were proposed by Groot and Warren.[24] The bond stretching force $\mathbf{F}_i^{B}$ was considered and calculated from the harmonic potential with a force constant of $4k_BT/r_c^2$ and an equilibrium length of 0.

Kacar *et al.*[12,13] constructed a parameterization scheme for each DPD particle with different densities based on its molecular structure, and Li *et al.*[14] extended this scheme to identify all the parameters using all-atom MD. In this study, we used this approach to identify the parameters of the SiHy components. Fig. 2 shows the coarse-graining procedure. For the relatively high-molecular-weight modified PDMS, coarse graining was performed using multiple beads. The terminal groups were divided into hydrophilic and hydrophobic units, and each unit was coarse-grained with a single bead. The PDMS part is a coarse-grained model of a 30–50 mer, where each bead represents a 5 mer (PDMSn5). These are connected by harmonic bonds, as shown in Fig. 2. TMSM and DMAA are coarse-grained monomers with single beads.

First, an all-atom model was created for each component based on the coarse-graining process shown in Fig. 2. Here, the cutting points of the PDMS parts (*e.g.*, the bond between nitrogen and cyclohexane at the R1–R2 junction) were terminated with hydrogen. We performed all-atom MD simulations for each single-component liquid system and calculated the density and solubility parameters of each component (see the SI[25–34]). We determined a_{ij} according to the procedure of Kacar *et al.* using the obtained density, solubility parameter, and ternary composition ratio. The obtained DPD parameters are summarized in Table 2. The cutoff distance, *i.e.*, the reference distance, r_c = 9.83 Å, and the reference temperature was 300 K.

3.2 Polymerization DPD simulation

We used the reactive DPD algorithm proposed in our previous study.[15,35] The reaction model has two criteria, as shown in Fig. S1. The first criterion concerns the distance between the reactive beads, where R1, TMSM, DMAA beads are reactive beads, and each bead can react twice. When the distance between the reactive beads was within the reaction cutoff, the bead pair became a reaction candidate. The reaction cutoff was set to $0.5r_c$ = 4.915 Å. The second criterion is the reaction probability, p_{react}, which was calculated using the Arrhenius equation as follows:

$$p_{react} = A \exp\left(-\frac{E_a}{RT}\right) \quad (7)$$

where E_a is the activation energy, R is the gas constant, and T is the local temperature calculated from the corresponding bead pair. The acceleration constant A required to reproduce the curing reaction within a realistic computational time was set to 10^7. A reaction occurs when p_{react} is greater than a uniformly distributed random number between 0 and 1, and a new harmonic bond is created between the corresponding two reactive beads. Subsequently, a DPD simulation was performed for structural relaxation. The actual materials undergo radical polymerization, and various reactions occur between the initiators and the radical/non-radical groups. In this coarse-grained simulation, the initiators and radical/non-radical groups were not distinguished, and the same reaction judgement algorithm was applied to all the reactive particles. In addition, depending on the combination of monomers, for example, PDMS/DMAA and TMSM/DMAA, the activation energy E_a has different values, *i.e.*, corresponding to the different reaction rates. In this composition, the reaction rate is almost the same experimentally; therefore, we used E_a = 3.73 kcal mol^{-1} for the self-

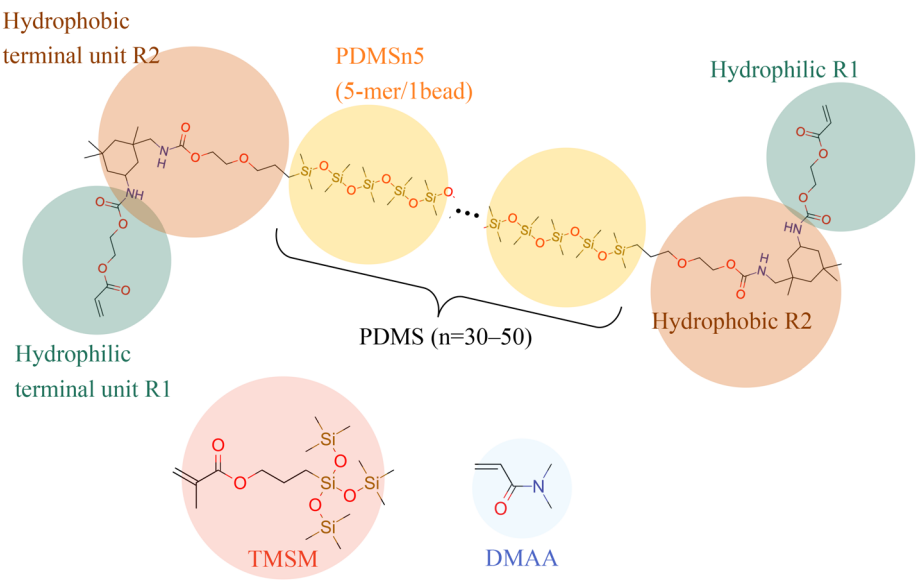

Fig. 2 Coarse-grained mapping of the monomer structures used in the reactive DPD model. Each monomer is represented by one or more beads and bonds. R1, TMSM, and DMAA beads are assigned as reactive sites in the polymerization scheme.

Table 2 Summary of the DPD parameters: density ρ [g cm^{-3}], solubility parameter δ [(J cm^{-3})$^{1/2}$], Flory–Huggins parameter χ_{ij}, and pairwise repulsion parameter a_{ij} [k_BT]

a_{ij} (χ_{ij})	PDMSn5 (ρ = 1.20) (δ = 18.7)	R1 (ρ = 1.16) (δ = 23.4)	R2 (ρ = 0.95) (δ = 18.49)	DMAA (ρ = 0.89) (δ = 20.06)	TMSM (ρ = 1.13) (δ = 18.78)
PDMSn5	98.59 (0)	37.74 (1.69)	76.74 (0.003)	26.56 (0.14)	96.39 (0.0005)
R1		11.16 (0)	31.85 (1.84)	14.25 (0.86)	36.92 (1.63)
R2			59.72 (0)	21.02 (0.19)	75.03 (0.006)
DMAA				6.94 (0)	25.94 (0.12)
TMSM					94.24 (0)

polymerization of DMAA[36] for all reactions. This approximation neglects monomer-pair-dependent reactivity ratios and the explicit distinction between radical and non-radical species. These simplifications may influence the predicted morphology and domain connectivity for systems with strongly different monomer reactivities. In such cases, more detailed reaction parameters would be required.

All DPD simulations were performed using LAMMPS,[37] and the reaction was evaluated using an external script. In the structural relaxation simulation using DPD, NPT simulations were performed in combination with a Berendsen barostat,[38,39] the temperature was set to the reference temperature ($1T$ = 300 K), and the pressure was set to $23.8k_BT/r_c^3$, which was used in the parameter identification.

3.3 Structural analysis

To obtain a quantitative understanding of the polymerization-induced phase-separation structure, we calculated the Faber–Ziman partial structure factor.[15,40] The periodic structure size can be obtained from the structural factor peak, which corresponds to the characteristic length scale evaluated by techniques such as FFT analysis of TEM images and SAXS. First, the partial radial distribution function $g_{\alpha\beta}(r)$ for each bead type was obtained as follows:

$$g_{\alpha\beta}(r) = \frac{N_{\alpha\beta}(r)}{4\pi r^2 n_\beta \mathrm{d}r} \tag{8}$$

where $N_{\alpha\beta}(r)$ is the number of pairs between species α and β within the distance from r to r + dr, and n_β is the average number density of species β. The Faber–Ziman partial structure factor can be obtained by Fourier transformation, as follows:[41]

$$S_{ij}^{\mathrm{FZ}}(q) = n_0 \int_0^\infty 4\pi r^2 \left(g_{ij}(r) - 1\right) \frac{\sin(qr)}{qr} \mathrm{d}r + 1 \tag{9}$$

where q is the length of the scattering vector and n_0 is the system number density.

3.4 Analysis of permeation through SiHy

In a binary system such as PDMS/DMAA, the hydrophilic domain, *i.e.*, the DMAA domain, and the hydrophobic domain, *i.e.*, the PDMS domain, within the phase-separated structure act as the primary routes for water/ions and oxygen, respectively, to permeate through the contact lenses. Therefore, it is necessary to quantitatively evaluate whether each domain is percolated and what the permeation properties of the tortuous route are.

The analysis was performed using a two-component system of PDMS/DMAA. First, the simulation domain was divided into voxels of approximately $0.5r_c$, and each voxel was binarized based on the particle density contained within it. The particle density was calculated by weighted accumulation, assigning a weight of 1 to the voxel containing the particle and 0.3 to each of the 26 neighboring voxels. The PDMSn5, R1, and R2 beads were counted as PDMS, the DMAA beads were counted as DMAA, and the voxels were binarized into the type with the highest final density. Fig. 3 illustrates an example of this procedure.

Next, we performed transport analysis using a random walk. Test particles were randomly inserted into the voxels at the

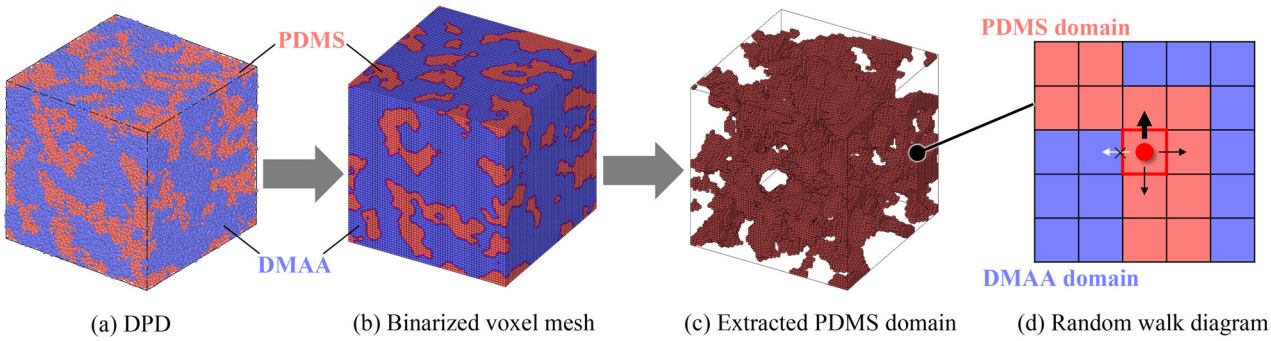

Fig. 3 Schematic of the conversion from DPD into a binary voxel mesh. (a) Phase-separated structure of PDMS/DMAA obtained from the DPD simulation, (b) binarization on a voxel mesh based on the particle density, and (c) extraction of the PDMS domain. (d) Conceptual diagram of the random walk of an oxygen test particle in the PDMS domain.

bottom as shown in Fig. 3(b). There were two types of test particles: one mimicking oxygen and the other mimicking water. The oxygen test particles can only pass through the PDMS domain, whereas the water test particles can only pass through the DMAA domain. If the initial position was in the other domain, *e.g.*, if the oxygen test particle was inserted into the DMAA domain, it was reinserted. Fig. 3(d) shows a conceptual diagram of this random walk. For simplicity, it is drawn in two dimensions. The test particle can move to neighboring voxels by moving up, down, left, right, front, and back. A random number is generated, which moves up with a probability of 2/7, and in other directions with a probability of 1/7. This difference in probability is introduced to represent advection owing to the density gradient from below to above. In addition, as shown in Fig. 3(d), it cannot move to a different type of domain (PDMS domain → DMAA domain). Accordingly, in this phase-confined random-walk transport analysis, a non-zero flux from the bottom to the top boundary necessarily implies the existence of a spanning connected pathway in the corresponding phase. The lower boundary is a specular reflection, the left and right boundaries are periodic, and the analysis is performed until the test particle reaches the upper boundary.

Based on the Brownian motion concept using a random walk, the diffusion coefficient in one direction can be estimated as $\langle x(t)^2\rangle/2t$ from the mean-square displacement $\langle x(t)^2\rangle$ of the particles and sampling time t. In the present analysis, we instead quantify transport using a first-passage-time metric: for test particles confined to domain i, we measure the travel time t_i required to reach the upper boundary from the lower boundary and define a permeability index,

$$D_i = \frac{L^2}{2\langle t_i\rangle}, \tag{10}$$

where L is the distance between the lower and upper boundaries (*i.e.*, the cell size) and $\langle t_i\rangle$ is the average travel time *via* domain i. If the entire simulation domain is composed of the same type of material, *i.e.*, there are no obstacles, the corresponding index is defined as D_0. The permeability of the phase-separated structures is then evaluated using the normalized index D_i/D_0.

4 Results and discussion

4.1 TEM observation

The TEM image of sample 1 (binary system with a PDMS : DMAA weight ratio of 8 : 2) and the corresponding FFT patterns calculated from the image are shown in the upper right panel of Fig. 4. The TEM images and FFT patterns for samples 2 and 3, which are also binary systems, are shown in Fig. S2. The domain sizes and scattering intensities extracted from the FFT patterns of samples 1–3 are shown in Fig. 4. Staining was applied to DMAA. The FFT analysis of the TEM images indicates a characteristic domain periodicity of approximately 10–20 nm. While 2D sections can suggest an interpenetrating domain morphology, the 3D connectivity cannot be uniquely determined from TEM slices alone. As the fraction of DMAA increased, the domain-to-domain spacing $d = 1/f$ observed in the TEM images exhibited a clear enlarging trend, with values of 12.2, 12.6, and 19.2 nm for samples 1, 2, and 3, respectively. This tendency is consistent with the behavior previously observed in SAXS measurements.[19]

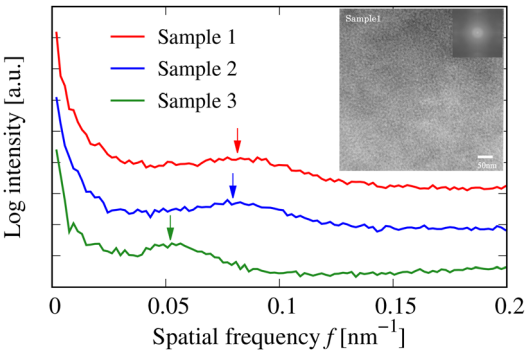

Fig. 4 TEM image of sample 1 and the corresponding two-dimensional FFT patterns calculated from the TEM micrographs. The FFT-derived size distribution profiles for samples 1–3 are also presented. The characteristic spacing was estimated from the spatial frequency f (cycles per nm) as $d = 1/f$. The TEM and FFT images of samples 2 and 3 are provided in the SI.

4.2 Structural analysis of binary systems using DPD simulation

Phase-separation simulations were performed for the PDMS/DMAA binary systems. As in experimental samples 1–3, the weight ratios of PDMS to DMAA were set to 80 wt% : 20 wt%, 60 wt% : 40 wt%, and 40 wt% : 60 wt%, respectively; the corresponding numbers of molecules were set to 10 240 : 117 248, 7680 : 234 432, and 5120 : 351 680. Fig. 5 shows the final phase-separated structures obtained for each composition, and Fig. 6 shows the intensity distributions of the PDMS–PDMS structure factor calculated from these structures using eqn (9). The phase-separation process is shown in the SI Video (PhaseSeparation-binary-DPD.mp4). During polymerization, PDMS and DMAA formed copolymers while developing an interpenetrating, network-like phase-separated morphology (*i.e.*, a bicontinuous-like structure in 3D). As the composition changed, the dominant domain transitioned from PDMS to DMAA, accompanied by a change in morphology. In Fig. 6, the intensity of the peak shifted to higher q values with increasing PDMS content, indicating that the representative domain size decreased. A similar trend was observed for the DMAA–DMAA structure factor. Specifically, the peak positions were $q = 0.626$, 0.514, and 0.483 nm^{-1} for samples 1–3, respectively, corresponding to $d = 2\pi/q = 10.04$, 12.23, and 13.00 nm. These tendencies and the domain size scale were consistent with the FFT analysis of the TEM images, as shown in Fig. 4 and previous SAXS measurements,[19] demonstrating that the present DPD simulation successfully reproduced the polymerization-induced phase-separation behavior of the SiHy. The peak intensity decreased with increasing PDMS content, which was attributed to the formation of a PDMS-rich bulk phase that reduced sensitivity to local structural features.

4.3 Three-dimensional structural observation of amphiphilic block copolymers

A 3D structural analysis of sample 4, a ternary amphiphilic block copolymer, was performed using electron tomography.

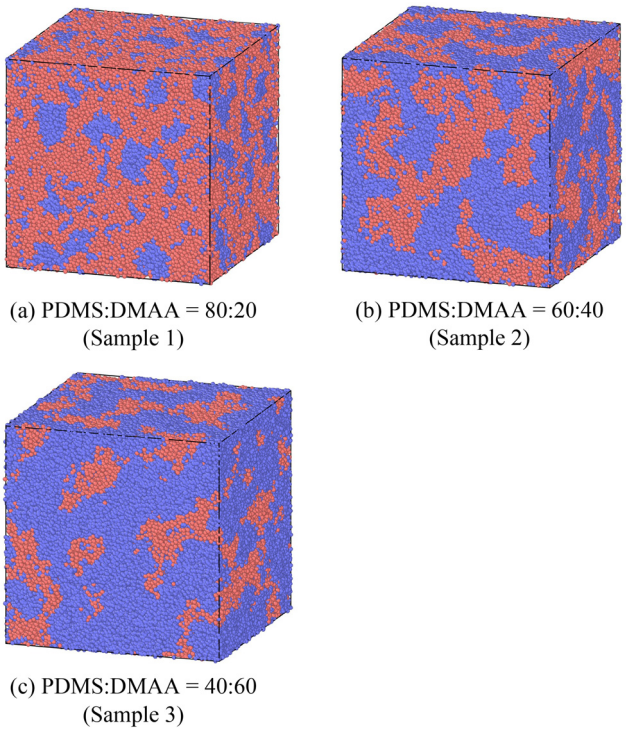

Fig. 5 Final phase-separated morphologies of the PDMS/DMAA binary systems obtained by reactive DPD simulations for the compositions corresponding to samples 1–3: (a) sample 1, PDMS:DMAA = 80:20; (b) sample 2, PDMS:DMAA = 60:40; and (c) sample 3, PDMS:DMAA = 40:60. Red and blue particles represent PDMS and DMAA, respectively.

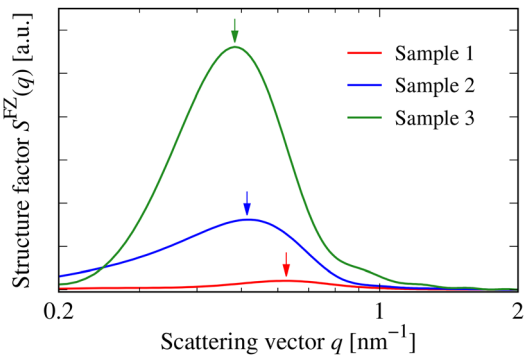

Fig. 6 Intensity profiles of the PDMS–PDMS partial structure factor $S^{FZ}(q)$ computed from the final morphologies (Fig. 5) for PDMS/DMAA binary systems with different compositions (samples 1–3). The peak position reflects the characteristic domain spacing ($d = 2\pi/q$), enabling comparison with the TEM/FFT-derived length scale (Fig. 4).

Tomographic images obtained from ultrathin sections collected within a tilt range of ±70° frequently exhibit artifacts caused by anisotropy that is not inherent to the sample, a phenomenon commonly known as the missing wedge problem.[22] To overcome this issue, a conical-shaped specimen was prepared, enabling the continuous rotation of the sample from 0° to 90° in the horizontal plane. Consequently, the reconstructed tomograms exhibited isotropic image resolution, allowing artifact-free observation of the 3D structure. However, owing to the longer staining time required compared to ultrathin sections, potential shrinkage of the specimen may have occurred, and caution is required when interpreting the measured values. Although ruthenium tetroxide staining was used for TEM observations of samples 1–3, the use of a 10% PTA solution enabled the construction of clearer tomograms even for the fine nanostructures present in sample 4. The sample was synthesized using two types of silicone compounds: high-molecular-weight PDMS and the monomer TMSM.[42] Traditionally, silicone compounds with strong mutual affinities have been assumed to aggregate and form hydrophobic domains. However, SAXS and SANS experiments indicated a strong likelihood that TMSM coexists with DMAA within the same domain.[20]

Fig. 7 shows the 3D TEM reconstruction of the ternary SiHy system (sample 4). Because PTA selectively stains the hydrophilic phase through its reaction with DMAA, the hydrophilic domains appear as stained regions in the tomogram. The reconstructed 3D volume revealed a stained-to-unstained volume ratio of approximately 2 : 1, indicating that the stained regions were present at approximately twice the volume of the unstained domains. This suggests that TMSM is located within DMAA-rich hydrophilic domains. This observation was consistent with the results obtained from the scattering experiments. Therefore, although TMSM traditionally interacts through its side chain and forms domains with PDMS,[43] both the scattering experiments and the present microscopic analysis demonstrate that TMSM instead forms domains together with DMAA. In addition, the 3D-TEM analysis suggested that both the stained and unstained regions formed continuous interconnected networks, indicating the presence of a co-continuous morphology. Because the present 3D-TEM reconstruction was obtained from one observed volume of sample 4, the quantitative volume ratio should be interpreted with caution in terms of statistical representativeness. Nevertheless, the reproducibility of the phase-separated morphology was confirmed by repeated 2D-TEM observations of the same material. In addition, the observed co-continuous morphology is consistent with the conclusions derived from SAXS and SANS measurements, including contrast-matching analyses, as well as with the numerical results discussed below. Therefore, the 3D-TEM result provides reasonable support for the bicontinuous structural interpretation.

4.4 Structural analysis of ternary systems using DPD simulation

A phase-separation simulation was performed for the ternary PDMS/DMAA/TMSM system corresponding to sample 4. The weight ratio of PDMS : DMAA : TMSM was set to 34 wt% : 33 wt% : 33 wt%, and the corresponding number of molecules was set to 5248 : 234 560 : 54 976. Fig. 8(a) shows the final phase-separated structure, along with cross-sectional views shown in (c) and (d). In the cross-sectional views at x = 20 and 30 nm, the structure is binarized based on the particle densities of PDMS (red particles) and DMAA (blue particles), and the neighboring TMSM particles (yellow) are classified according to the domain to which they belong. In the previous section, 3D TEM analysis suggested that TMSM tended to coexist with DMAA rather than

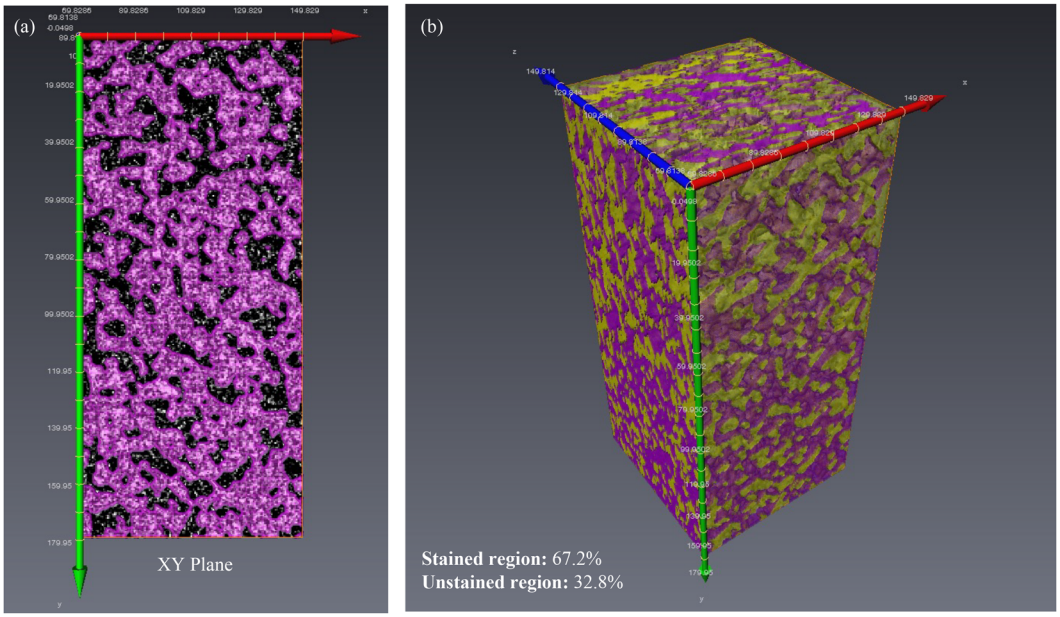

Fig. 7 Microphase-separated structure of the rod-shaped specimen of the SiHy ternary system (sample 4) obtained from 3D-TEM analysis STEM tomography reconstruction. Stained and unstained regions are shown in purple and yellow, respectively. (a) *xy* plane view of stained domains. (b) 3D rendering of the reconstructed volume showing both the stained and unstained domains. The volume ratio of stained-to-unstained regions was estimated to be approximately 2 : 1.

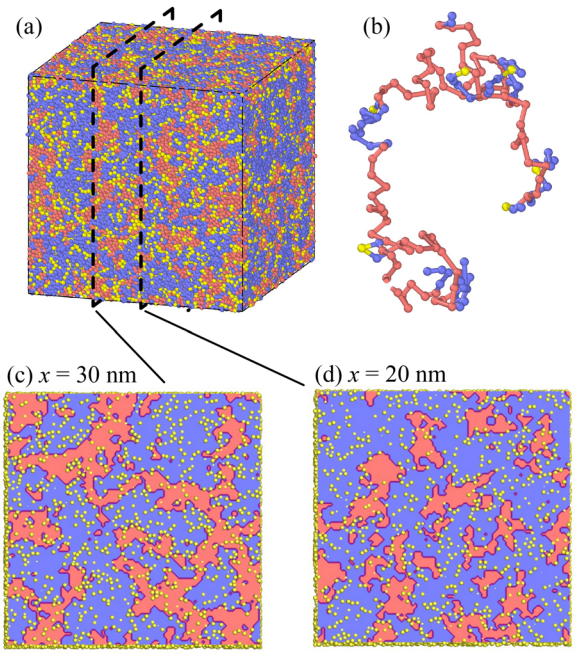

Fig. 8 (a) Final phase-separated structure for the ternary system. Red, blue, and yellow particles represent PDMS, DMAA, and TMSM, respectively. (b) Snapshot of the copolymer. (c)–(d) Cross-sectional images of the binarized PDMS/DMAA and the TMSM particles.

PDMS (Fig. 7), even though PDMS and TMSM are silicon-based components. In the cross-sectional images shown in Fig. 8(c) and (d), many TMSM particles belong to the DMAA domain. When the domain affiliation of all TMSM particles was quantified, approximately 80% of TMSM was found to be located within the DMAA domain. Therefore, these DPD simulation results corroborate the coexistence of TMSM and DMAA, as suggested by the 3D TEM analysis.

Fig. 9 shows the monomer-level reaction rate with respect to the overall reaction rate. The terminal groups of PDMS were hydrophilized, exhibiting a high affinity for DMAA. As a result, DMAA, which has a larger number of molecules and readily undergoes both self-polymerization and copolymerization, reacted most rapidly, followed by PDMS. In contrast, the reaction of TMSM proceeded much more slowly, and its reaction rate remained at approximately 50%, even at the final stage. This indicated that many TMSM molecules reacted only once at the terminal position or remained unreacted. Although TMSM is highly miscible with the internal silicon part of PDMS (PDMSn5

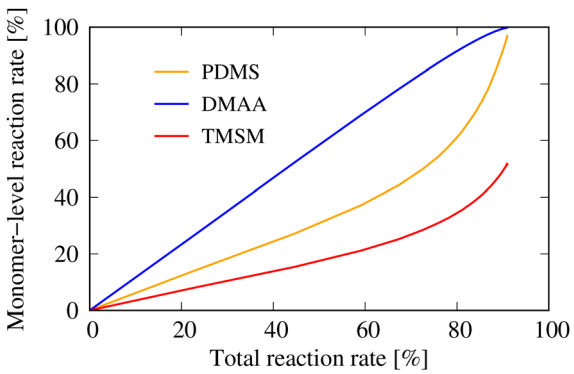

Fig. 9 Monomer-level reaction rate relative to the overall reaction rate in the reactive DPD simulation. The plot highlights the relative reactivity of the monomers during PIPS.

and R2 particles), it is poorly compatible with the terminal reactive groups (R1 particles). Consequently, reactions involving TMSM proceed slowly because its reactive groups cannot readily approach those of other monomers. TMSM polymerizes between the PDMS–DMAA copolymer chains and, as a result, tends to be incorporated into the DMAA segments. Fig. 8(b) shows a snapshot of a representative molecule at an overall conversion of 75%. Although the product was a ternary copolymer composed of PDMS, DMAA, and TMSM, most of the TMSM units were incorporated into the DMAA segments. This provides a mechanistic explanation for the formation of the DMAA/TMSM coexistence region, and this interpretation is further supported by kinetic considerations based on the previously reported SAXS data.[20]

4.5 Discussion on physical transportation

The formation of bicontinuous phase-separated structures is expected to enable selective mass transport, in which distinct molecular species traverse separate phase-specific pathways. To explore this concept, we conducted both experimental measurements and numerical simulations to analyze the transport properties of the system.

In simple hydrogel membranes, water-soluble species are transported through an aqueous phase *via* dissolution and diffusion. Therefore, an increase in water content generally leads to enhanced permeability. This phenomenon is well explained by the free-volume theory, which posits that molecular diffusion is facilitated by the available free volume in the medium.[23] Historically, hydrogel membranes have been adopted as contact lens materials to ensure oxygen permeability of the cornea *via* the free volume of water. In contrast, silicone-based compounds such as PDMS and silyl groups are known for their high molecular mobility and excellent gas permeability. In SiHy materials, the contribution of the silicone phase to oxygen permeability significantly exceeds that of the aqueous phase, highlighting the dominant role of the silicone network in gas transport. To verify this, we investigated oxygen permeability as a representative transport property of the silicone phase, and sodium ion permeability as a representative of the hydrophilic phase using PDMS-DA/DMAA binary copolymer systems. The experimental results are presented in Fig. 10.

4.5.1 Oxygen permeability. An increase in PDMS content led to a clear enhancement in oxygen permeability, whereas an increase in the DMAA content resulted in reduced oxygen permeability. These observations confirm that oxygen transport is predominantly facilitated by the silicone-rich phase, which provides a low-resistance pathway for gas molecules owing to its high free volume and molecular mobility.

4.5.2 Sodium ion permeability. The transport of sodium ions, which is highly dependent on the presence of water, increased with increasing DMAA content—corresponding to higher hydrophilicity and water uptake. This indicates that sodium ion transport occurs primarily through the hydrophilic domains, where water molecules enable ion diffusion.

4.5.3 Implications for functional phase separation. The simultaneous enhancement of oxygen permeability with increasing PDMS content and of sodium ion permeability with increasing DMAA content strongly suggests that each phase plays a distinct functional role in mass transport. These findings provide experimental evidence that bicontinuous phase-separated structures in SiHy materials facilitate phase-specific transport pathways, enabling the independent optimization of oxygen and ion permeability—critical features of next-generation contact lens materials.

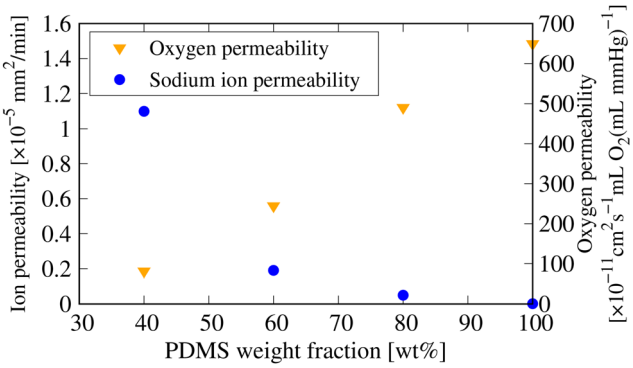

Fig. 10 Oxygen and sodium ion permeability coefficients of PDMS-DA/DMAA two-component membranes as functions of the PDMS-DA weight ratio. The oxygen permeability coefficient increased with increasing PDMS-DA weight ratio, while the sodium ion permeability coefficient increased with decreasing PDMS-DA weight ratio, *i.e.*, increasing DMAA weight ratio. Regarding the ion permeability coefficient, the reported values[44] were reanalyzed and are presented in this study.

Although permeability generally reflects both solubility and diffusivity, the composition-dependent trends for a given probe (O_2 or Na^+) measured in the same membrane series are primarily expected to reflect changes in the accessible transport pathways, provided that transport is dominated by phase-selective routes. In this context, the key question is whether the observed permeability trends can be accounted for by the pathway volume fraction alone or whether pathway geometry/topology (*e.g.*, connectivity and tortuosity) plays a decisive role. To address this point, we perform domain-restricted transport analyses on the DPD-generated morphologies, which isolate the geometric contribution of the phase-separated pathways and enable a direct comparison with the experimental composition-dependent trends.

4.5.4 Simulated permeability. Fig. 11 shows the simulated permeability index as a function of the PDMS weight fraction. Each permeability index was normalized by the reference D_0, obtained from a random-walk simulation in an obstacle-free domain using the same step rule as in the domain-restricted calculations. The reference D_0 is identical for the single-component limits (100 wt% PDMS and 100 wt% DMAA) because it is defined on an obstacle-free voxel model. Test particles were constrained to move within either the PDMS domain or the DMAA domain. Under all conditions, particles in each domain traversed the simulation box, confirming that both domains formed continuous pathways in the phase-separated structure. As the PDMS weight fraction increased, the permeability index on the PDMS side increased, corresponding to the experimentally observed increase in oxygen permeability. In contrast, the permeability index on the DMAA side decreased, corresponding to the experimentally observed decrease in ion permeability (Fig. 10). The simulated permeability index should not be

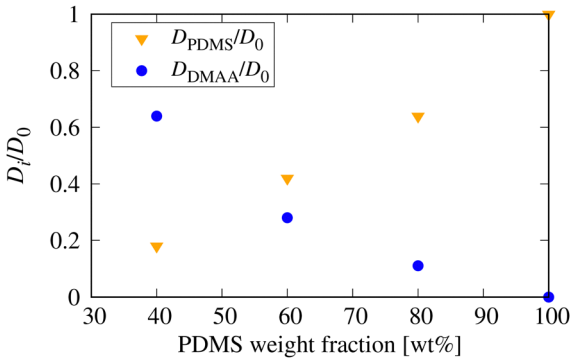

Fig. 11 Simulated permeability index, expressed as the normalized diffusivity D/D_0, for test-particle transport confined to the PDMS or DMAA domains in the phase-separated structures obtained by reactive DPD. The PDMS- and DMAA-domain indices correspond to transport through the hydrophobic and hydrophilic pathways, respectively, as compared with the experimental trends shown in Fig. 10.

regarded as a quantitative prediction of the experimental permeabilities, which include both solubility and diffusivity contributions. Rather, it represents the geometric contribution of phase-specific pathways, such as connectivity and tortuosity. Therefore, we compare the simulations and experiments only in terms of composition-dependent trends.

To further quantify how pathway geometry affects transport beyond the domain volume fraction, we evaluate the tortuosity of each percolating domain as described below. Following theoretical models for diffusion in porous media,[45–48] the permeability index D_i through domain i can be related to the reference D_0, the volume fraction ϕ_i, and the tortuosity τ_i as

$$\frac{D_i}{D_0} = \frac{\phi_i}{\tau_i}. \tag{11}$$

Accordingly, the tortuosity of domain i is evaluated using $\tau_i = \phi_i D_0/D_i$, which enables separation of the reduction in permeability arising from the decreased accessible pathway volume from that arising from increased pathway convolution. Fig. 12 summarizes the domain volume fractions and the corresponding tortuosities, where ϕ was obtained from the voxel mapping.

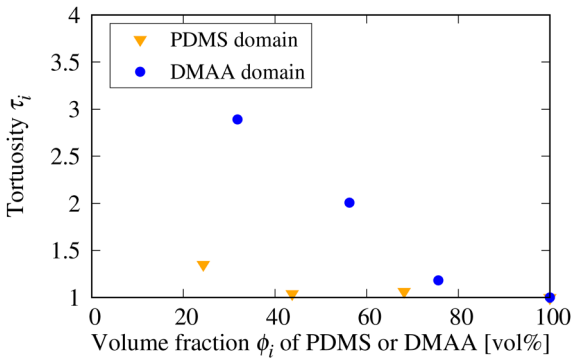

Fig. 12 Relationship between the domain tortuosity τ_i and volume fraction ϕ_i for the PDMS and DMAA domains. Higher tortuosity corresponds to more convoluted pathways; at low contents, PDMS pathways remain relatively straight, whereas DMAA pathways become highly tortuous.

Distinct trends were observed for the two domains. For the PDMS domain, τ remained close to unity even when the PDMS volume fraction decreased. This trend suggests that comparatively stable and relatively straight transport pathways can be maintained even at a low PDMS content, possibly reflecting the larger molecular structure of the PDMS monomer. In contrast, the DMAA-rich domain exhibited a sharp increase in τ at low ϕ_{DMAA}, suggesting the formation of highly tortuous pathways, which would suppress water/ion transport. This behavior may reflect the comparatively small DMAA monomer, which can lead to thinner and less robust pathways in copolymer networks with low DMAA content.

Overall, performing transport analysis on the phase-separated morphologies obtained from DPD simulations demonstrates that the composition–pathway-shape relationship depends on the constituent species, and this difference in pathway tortuosity contributes to the observed permeability trends.

5 Conclusion

In this study, the 3D structure and transport functionality of an amphiphilic copolymer composed of hydrophilic and hydrophobic phases were investigated using a combination of experimental and computational approaches. Experimentally, structural analyses were performed using TEM, and the results were compared with the morphologies previously inferred from SAXS measurements. 3D TEM reconstruction provided further insights into the nanoscale arrangement and connectivity of the domains. In addition, permeability measurements of the species migrating predominantly through the hydrophilic and hydrophobic phases (using sodium ions and oxygen, respectively) enabled a domain-resolved evaluation of molecular transport. Complementarily, numerical analyses were conducted by first determining the characteristic molecular parameters in a bottom-up manner based on all-atom MD simulations, followed by DPD simulations to model the structure-formation process of the amphiphilic copolymer. The simulated morphologies closely reproduced those observed in the TEM experiments, and domain-restricted transport simulations captured the composition-dependent migration trends within each phase. Importantly, the results indicate that the observed phase-selective transport cannot be explained solely by changes in the domain volume fraction; differences in pathway geometry (*e.g.*, tortuosity) between the two domains make a key contribution to the transport selectivity, and these geometric differences depend on the constituent monomer species. Overall, this experimentally validated multiscale framework links PIPS-driven co-continuous morphology to phase-selective transport *via* domain connectivity and pathway tortuosity, providing a basis for mechanistic interpretation and simulation-guided materials design.

Author contributions

Conceptualisation: EI, YK, and TO; methodology: EI and YK; validation: EI, YK, and TO; formal analysis: EI and YK; investigation: EI and YK; resources: EI and TO; data curation: EI and

YK; writing – the original draft: EI and YK; writing – review & editing: EI, YK, and TO; visualization: EI and YK; supervision: TO; project administration: TO; and funding acquisition: EI and TO.

Conflicts of interest

There are no conflicts to declare.

Data availability

The supporting data have been provided as part of the supplementary information (SI). Supplementary information: PhaseSeparation-binary-DPD.mp4: phase-separated structure formation obtained by DPD simulation for samples 1–3. PhaseSeparation-ternary-DPD.mp4: phase-separated structure formation obtained by DPD simulation for sample 4. 3DTEM_slice_x_y_z.mp4: slice image of 3D TEM for sample 4. Y_axis_rotation.mp4: rotation image of 3D TEM for sample 4. SupplementaryMaterials.pdf: supplementary materials on experiments and numerical analysis. See DOI: https://doi.org/10.1039/d6sm00092d.

Acknowledgements

The authors gratefully acknowledge Prof. Katsuhiro Yamamoto (Faculty of Engineering, Shinshu University) for his valuable advice on correlating the SAXS and TEM results. We also thank Dr Hiroshi Takase (Nagoya City University, School of Medicine) for his support with the ultrathin cryosectioning for TEM and Dr Yoshikazu Sasaki (JEOL Ltd) for his assistance with 3D tomography. Part of this study used the multiscale simulation platform CoSMIC (https://www.cosmic.plum.mech.tohoku.ac.jp/english.html). Numerical simulations were performed using the supercomputing resources at the Cyberscience Center, Tohoku University.

References

1 L. Xiang, Q. Li, C. Li, Q. Yang, F. Xu and Y. Mai, *Adv. Mater.*, 2023, **35**, 1–28.
2 J. J. Hernandez, H. Zhang, Y. Chen, M. Rosenthal, M. D. Lingwood, M. Goswami, X. Zhu, M. Moeller, L. A. Madsen and D. A. Ivanov, *Macromolecules*, 2017, **50**, 5392–5401.
3 S. D. Xu, S. Gu, X. L. Pu, Y. F. Xiao, J. H. Lu, Y. Z. Wang and L. Chen, *Composites, Part B*, 2022, **247**, 110326.
4 Q. Tran-Cong-Miyata and H. Nakanishi, *Polym. Int.*, 2017, **66**, 213–222.
5 B. E. McKenzie, J. F. De Visser, G. Portale, D. Hermida-Merino, H. Friedrich, P. H. Bomans, W. Bras, O. R. Monaghan, S. J. Holder and N. A. Sommerdijk, *Soft Matter*, 2016, **12**, 4113–4122.
6 E. Reister, M. Müller and K. Binder, *Phys. Rev. E*, 2001, **64**, 17.
7 D. J. Grzetic and R. A. Wickham, *J. Chem. Phys.*, 2020, **152**, 104903.
8 C. Li and A. Strachan, *Polymer*, 2018, **149**, 30–38.
9 M. M. Henry, S. Thomas, M. Alberts, C. E. Estridge, B. Farmer, O. McNair and E. Jankowski, *Polymers*, 2020, **12**, 1–19.
10 P. V. Coveney and K. E. Novik, *Phys. Rev. E*, 1996, **54**, 5134–5141.
11 H. Liu, H. J. Qian, Y. Zhao and Z. Y. Lu, *J. Chem. Phys.*, 2007, **127**, 144903.
12 G. Kacar, E. A. Peters and G. De With, *EPL*, 2013, **102**, 40009.
13 G. Kacar, E. A. Peters and G. De With, *Soft Matter*, 2013, **9**, 5785–5793.
14 K. Li, G. Kikugawa, Y. Kawagoe, Y. Zhao and T. Okabe, *Soft Matter*, 2024, **20**, 4591–4607.
15 Y. Kawagoe, G. Kikugawa, K. Shirasu, Y. Kinugawa and T. Okabe, *J. Phys. Chem. B*, 2024, **128**, 2018–2027.
16 Y. Kinugawa, Y. Kawagoe, K. Shirasu and K. Ryuzono, *Int. J. Mech. Sci.*, 2025, **306**, 110779.
17 C. C. Peng and A. Chauhan, *J. Membr. Sci.*, 2012, **399–400**, 95–105.
18 K. Xu, *Highl. Sci. Eng. Technol.*, 2025, **125**, 197–202.
19 K. Yamamoto, E. Ito, S. Fukaya and H. Takagi, *Macromolecules*, 2009, **42**, 9561–9567.
20 K. Yamamoto, E. Ito and Y. Mori, *Macromol. Symp.*, 2019, **385**, 1–5.
21 Y. Yokoyama, *et al.*, *EP0584764*, 1993.
22 H. Jinnai and R. J. Spontak, *Polymer*, 2009, **50**, 1067–1087.
23 H. Yasuda, C. E. Lamaze and A. Peterlin, *J. Polym. Sci., Part A-2*, 1971, **9**, 1117–1131.
24 R. D. Groot and P. B. Warren, *J. Chem. Phys.*, 1997, **107**, 4423–4435.
25 C. Li and A. Strachan, *Polymer*, 2018, **135**, 162–170.
26 S. L. Mayo, B. D. Olafson and W. A. Goddard III, *J. Phys. Chem.*, 1990, **94**, 8897–8909.
27 A. K. Rappé and W. A. Goddard, *J. Phys. Chem.*, 1991, **95**, 3358–3363.
28 Y. Wang, Y. Shi, Q. Sun, K. Lu, M. Kubo and J. Xu, *J. Phys. Chem. C*, 2020, **124**, 10007–10015.
29 T. Okabe, T. Takehara, K. Inose, N. Hirano, M. Nishikawa and T. Uehara, *Polymer*, 2013, **54**, 4660–4668.
30 Y. Kawagoe, Y. Kinugawa, K. Matsumoto, M. Ohno, N. Kishimoto, T. Kawai and T. Okabe, *Phys. Chem. Chem. Phys.*, 2024, **26**, 24250–24260.
31 Y. Kawagoe, G. Kikugawa, S. Komori, K. Shirasu and T. Okabe, *Thermochim. Acta*, 2025, **747**, 179949.
32 Y. Xi, H. Fukuzawa, S. Fukunaga, G. Kikugawa, Y. Zhao, Y. Kawagoe, T. Okabe and N. Kishimoto, *Mol. Catal.*, 2024, **552**, 113680.
33 Y. Kawagoe and T. Okabe, *Comput. Mater. Sci.*, 2023, **228**, 112333.
34 N. Odagiri, K. Shirasu, Y. Kawagoe, G. Kikugawa, Y. Oya, N. Kishimoto, F. S. Ohuchi and T. Okabe, *J. Appl. Polym. Sci.*, 2021, **138**, 50542.
35 Y. Kawagoe, G. Kikugawa, K. Shirasu and T. Okabe, *Soft Matter*, 2021, **17**, 6707–6717.
36 J. Schrooten, I. Lacík, M. Stach, P. Hesse and M. Buback, *Macromol. Chem. Phys.*, 2013, **214**, 2283–2294.
37 S. Plimpton, *J. Comput. Phys.*, 1995, **117**, 1–19.

38 Y. Lin, D. Pan, J. Li, L. Zhang and X. Shao, *J. Chem. Phys.*, 2017, **146**, 124108.
39 H. J. Berendsen, J. P. Postma, W. F. Van Gunsteren, A. Dinola and J. R. Haak, *J. Chem. Phys.*, 1984, **81**, 3684–3690.
40 T. E. Faber and J. M. Ziman, *Philos. Mag.*, 1965, **11**, 153–173.
41 S. V. Kallivokas, A. P. Sgouros and D. N. Theodorou, *Soft Matter*, 2019, **15**, 721–733.
42 P. C. Nicolson and J. Vogt, *Biomaterials*, 2001, **22**, 3273–3283.
43 P. C. Nicolson, *et al.*, *US5760100*, 1998.
44 E. Ito, M. Higuchi, K. Yamamoto, K. Nagata and T. Kinoshita, *J. Appl. Polym. Sci.*, 2011, **120**, 79–85.
45 J. A. Currie, *Sorption and transport processes in soils*, 1970, pp. 152–171.
46 F. R. Troeh, J. D. Jabro and D. Kirkham, *Geoderma*, 1982, **27**, 239–253.
47 B. Ghanbarian, A. G. Hunt, R. P. Ewing and M. Sahimi, *Soil Sci. Soc. Am. J.*, 2013, **77**, 1461.
48 Y. Kawagoe, T. Oshima, K. Tomarikawa, T. Tokumasu, T. Koido and S. Yonemura, *Microfluid. Nanofluid.*, 2016, **20**, 162.

